AGU PUBLICATIONS

JGR

Journal of Geophysical Research: Atmospheres

RESEARCH ARTICLE
10.1002/2016JD025211

Mars' atmosphere: The sister planet, our statistical twin

Wilbur Chen[1], **Shaun Lovejoy**[1], **and Jan-Peter Muller**[2]

[1]Department of Physics, McGill University, Montreal, Quebec, Canada, [2]Mullard Space Science Laboratory, Department of Space and Climate Physics, UCL, Surrey, UK

Abstract Satellite-based Martian reanalyses have allowed unprecedented comparisons between our atmosphere and that of our sister planet, underlining various similarities and differences in their respective dynamics. Yet by focusing on large scale structures and deterministic mechanisms they have improved our understanding of the dynamics only over fairly narrow ranges of (near) planetary scales. However, the Reynolds numbers of the flows on both planets are larger than 10^{11} and dissipation only occurs at centimetric (Mars) or millimetric scales (Earth) so that over most of their scale ranges, the dynamics are fully turbulent. In this paper, we therefore examine the high-level, statistical, turbulent laws for the temperature, horizontal wind, and surface pressure, finding that Earth and Mars have virtually identical statistical exponents so that their statistics are very similar over wide ranges. Therefore, it would seem that with the exception of certain aspects of the largest scales (such as the role of dust in atmospheric heating on Mars, or of water in its various phases on Earth), that the nonlinear dynamics are very similar. We argue that this is a prediction of the classical laws of turbulence when extended to planetary scales and that it supports our use of turbulent laws on both planetary atmospheres.

Key Points:
- We compare the atmospheric statistics on Earth and on Mars
- We find that the Martian atmosphere exhibits similar scaling properties to the Earth's atmosphere
- We conduct a multifractal analysis and find similar results for the Martian and Earth atmospheres

Correspondence to:
S. Lovejoy,
lovejoy@physics.mcgill.ca

Citation:
Chen, W., S. Lovejoy, and J.-P. Muller (2016), Mars' atmosphere: The sister planet, our statistical twin, *J. Geophys. Res. Atmos.*, *121*, 11,968–11,988, doi:10.1002/2016JD025211.

Received 11 APR 2016
Accepted 6 SEP 2016

1. Introduction

Although modern atmospheric science has its origins in attempts to understand the Earth's atmosphere, thanks to satellite data and computer models, it has been extended to encompass extraterrestrial atmospheres, the most similar being on Mars. So far, the comparisons have focused on the similarities and differences of various dynamical mechanisms (see, e.g., the review by *Leovy* [2001]) and the Martian point of comparison has enriched our understanding of the Earth. Significant differences between terrestrial and Martian atmospheres include the strong control of Martian atmospheric temperature by dust, the larger role of topography, the stronger diurnal and annual cycles, and the larger role of atmospheric tides. Significant similarities include jets, zonal circulation patterns, and the existence of fairly similar Hadley cells.

These deterministic mechanisms are pertinent at the very largest spatial scales, but what about the rest? On both Mars and Earth, typical Reynolds numbers are greater than 10^{11} (Table 1), so that from planetary down to dissipation scales (centimetric and millimetric, respectively, Table 1) the flow is turbulent so that we would expect high-level (statistical) turbulent laws to be obeyed. As reviewed in *Lovejoy and Schertzer* [2013], these laws are of the form: $\Delta I(\Delta\bar{r}) \approx \phi\Delta\bar{r}^{H}$, where ΔI is a fluctuation in the parameter I, $\Delta\bar{r}$ is the vector separating two points, and ϕ a turbulent flux (or a power of a turbulent flux). For example, we recover the Kolmogorov law if I is a velocity component, $\Delta\bar{r}$ is the distance between two points, $\phi = \epsilon^{1/3}$ where ϵ is the energy flux to smaller scales, H is a scaling exponent, and the fluctuation $\Delta I(\Delta\bar{r})$ is taken as the difference in I between two points separated by vector $\Delta\bar{r}$ (in cases where $H < 0$, other definitions of fluctuations are needed). For atmospheric applications, the main limitations of the classical laws are their assumption that the turbulent flux is fairly homogeneous (constant or quasi-Gaussian) and that the turbulence is statistically isotropic: they take $\Delta\bar{r}$ to be the usual vector norm of the vector displacement $\Delta\bar{r}$. However, since the 1980s the development of multiplicative cascades to account for intermittency have allowed the fluxes to be wildly variable (multifractal), and the development of generalized scale invariance has allowed the turbulent laws to be extended beyond isotropy to strongly stratified flows. The resulting anisotropic cascade picture has been shown to be highly accurate for the Earth's atmosphere, numerical models of the atmosphere, and atmospheric reanalyses with significant deviations only occurring at scales larger than about 5000 km (see the extensive review by *Lovejoy and Schertzer* [2013]).

(A note on terminology: In this paper we use the term "stratification" to refer to vertical stratification, which is apparently scaling with different exponents in the horizontal and vertical direction implying that the

Table 1. Mars Versus Earth, Turbulent Characteristics Near Their Surfaces

	Earth	Mars
Density[a](ρ) (surface, kg/m^3)	1.24 (10°C)	7×10^{-3} (−20°C)
Dynamic viscosity[b](η), (kg m^{-1}s^{-1})	1.8×10^{-5} (10°C)	1.3×10^{-5} (−20°C)
Kinematic viscosity ($v = \eta/\rho$), m^2/s	1.5×10^{-5}	1.9×10^{-3}
L_w[c]	2×10^7	1.07×10^7
ΔU[d]	27	70
$Re = L_w \Delta U / v$	4×10^{13}	4×10^{11}
ϵ[e](W/kg = m^2/s^3)	10^{-3}	4×10^{-2}
L_{diss}[f] (m)	1.4×10^{-3}	2.0×10^{-2}

[a] The density was taken at the surface pressure (for Mars, 5 mb was used, for Earth, 1000 mb) and at 10°C Earth and −20°C Mars.

[b] The dynamic viscosity is nearly independent of pressure.

[c] Half the circumference, the largest great circle distance = πR where R is the planetary radius.

[d] ΔU taken from *Lovejoy et al.* [2014] (from reanalyses, average antipodes wind differences).

[e] The flux of turbulent energy to smaller scales (equal to the energy rate density) as estimated in *Lovejoy and Schertzer* [2011] (Earth) and *Lovejoy et al.* [2014] (Mars).

[f] The dissipation (Kolmogorov) scale estimated by using the Kolmogorov formula: $V_{\mathrm{diss}} = \epsilon^{1/3} L_{\mathrm{diss}}$ and the relation $Re_{\mathrm{diss}} = L_{\mathrm{diss}} V_{\mathrm{diss}} / v = 1$ to obtain: $L_{\mathrm{diss}} = (v^3/\epsilon)^{\frac{1}{4}}$.

stratification becomes more and more extreme at large scales. However, we find that there is an exactly (mathematically) analogous scaling anisotropy in the EW versus NS direction, and this is important in this paper. Also, in the following, we use the word scaling as in the physics literature, to refer to a physical quantity that varies in a power law way as a function of space and/or time scale. The corresponding exponents are "scale invariant" and the notion of scale can be considerably generalized from the usual Euclidean notion so as to take into account anisotropy.)

The advantage of these high-level laws is that although they describe the statistical properties over wide ranges of space-time scales, they are quite simple, and they provide the theoretical basis of stochastic modeling and stochastic forecasting [e.g., *Lovejoy et al.*, 2015]. Theoretically, the reason that the turbulent laws are obeyed is because the dynamic equations are formally scale invariant down to the dissipation scale. We therefore *expect* them to hold on Mars as well as Earth, although the relevant fluxes and exponents could be different. *Lovejoy et al.* [2014] took the first step in making a statistical Earth-Mars comparison by showing that with the exception of the diurnal and annual cycles and harmonics that the second-order temporal statistics (the spectra) for wind and temperature of the two planets were virtually the same, as long as the Martian time scales were rescaled by a factor of about 5, itself theoretically predicted from turbulence theory and from the differences in the overall solar forcing and atmospheric thicknesses. *Lovejoy et al.* [2014] used both in situ (Viking Lander) data and MACDA (Mars Analysis Correction Data Assimilation) reanalyzes [*Montabone et al.*, 2014]; the aim of this paper is to extend this statistical analysis to moments other than the second, to the pressure and both horizontal wind components, to provide analyses in space and in time, and finally to directly analyze turbulent fluxes and hence cascades structures. The methods are the same as those that were applied to terrestrial reanalyses in *Lovejoy and Schertzer* [2011]. Beyond establishing striking quantitative and qualitative similarities between Martian and terrestrial atmospheric variability, this paper underlines the importance of going beyond deterministic mechanistic descriptions to consider the simple higher level statistical laws needed for an understanding—and improved modeling—over a much wider range of space-time scales.

Let us briefly comment on turbulent fluxes which are fluxes in Fourier, not real space (i.e., across surfaces in Fourier space i.e. across scales). It seems that the energy flux is important in both for determining the horizontal velocity dynamics, whereas the buoyancy force variance flux controls the vertical structure of the horizontal wind. These are anisotropic generalizations of the classical Kolmogorov and Bolgiano-Obukhov laws. But most of the exponents observed in the atmosphere have yet to be explained and the corresponding fluxes identified. Fortunately, this is not necessary for analyzing the data and for estimating their intermittency characteristics.

This paper is organized as follows. In section 2, we describe the MACDA reanalysis data set used for the statistical analysis for the Martian Atmosphere. In section 3, we compare the Fourier-space spectral scaling of atmospheric fields on Earth and Mars. In section 4, we compare real-space statistics of atmospheric fields on Earth and Mars. In section 5, we discuss and conclude.

2. The Data

2.1. Martian Meteorology

The first general circulation model (GCM) of the Martian atmosphere was proposed by *Leovy and Mintz* [1969] by adapting the terrestrial GCM from the University of California, Los Angeles (UCLA) [*Mintz*, 1965]. The predictions of this model informed much of our initial understanding of the Martian atmosphere, in particular, the CO_2 condensation behavior in the atmosphere and the basic characteristics of the Martian circulation. With data from the Mars missions in the 1970s, significant improvements were made to this model at the NASA Ames Research Centre [see *Pollack et al.*, 1976; *Hollingsworth and Barnes*, 1996] and these improvements led to further theoretical refinements. In the following years, several other terrestrial models were adapted to Mars, furthering our understanding of the mechanics of the Martian atmosphere. For example, *Hourdin* [1992] and *Hourdin et al.* [1993] developed a model to explain the pressure variation of the Martian atmosphere, from an adaptation of the Laboratoire de Météorologie Dynamique (LMD) terrestrial model [*Morcrette et al.*, 1986]. Additionally, *Wilson and Hamilton* [1996] developed a model from the Geophysical Fluid Dynamics Laboratory (GFDL) terrestrial GCM [*Holloway and Manabe*, 1971], to explain the role of thermal tides.

In spite of the great strides in our understanding of Martian atmospheric dynamics at the largest scales, there has been little insight into the corresponding statistics needed to understand the dynamics over a wide range of space-time scales. An important reason has been the lack of high quality global scale Martian atmospheric data. However, with the development of a reanalysis product — the Mars Analysis Data Correction Assimilation (MACDA) *Montabone et al.* [2014] — detailed analysis of Martian atmospheric statistics is now possible.

2.2. Martian Reanalyses

The MACDA reanalysis is a hybrid of observational data and the data assimilation part of a numerical weather model. The observational data assimilated by MACDA were taken from the Thermal Emission Spectrometer (TES) [*Christensen et al.*, 2001] aboard the Mars Global Surveyor (MGS) at an average orbital height of 400 km. The TES measures thermal radiance via a combination of a spectrometer and two bolometers (one thermal and one near infrared). When combined, these instruments captured the thermal radiance of the Martian surface with 18 channels. Although, thermal emission spectra may be used to retrieve temperature and dust opacities using inversion algorithms (see *Smith et al.*, 2000 and *Conrath et al.* [2000] for dust opacity and temperature, respectively), the reanalysis allows them to be used more directly in a forward mode.

MACDA is based on a GCM developed in collaboration between (LMD) and the Department of Atmospheric, Oceanic and Planetary Physics at Oxford University (AOAP) (see *Forget et al.* [1999] for model specifications). The assimilation was first reported by *Lewis et al.* [2007], who used a scheme developed by the Meteorological Office in the U.K. [see *Lorenc et al.*, 1991]. The final reanalysis product, presented by *Montabone et al.* [2014], is a high quality data set (see, e.g., *Lewis et al.* [2016] for insights into the quality of the data set) that consists of seven Martian atmospheric fields, of which four were considered as thermodynamically and dynamically relevant for analysis — temperature, zonal (EW)/meridional (NS) wind, and surface pressure.

Each of the four atmospheric fields is gridded with a resolution of 5° ($\approx$300 km) and sampled at a frequency of 2 Martian hours (2×1.0275 Earth hours) over a period of 3 Martian years ($\approx$5.64 Earth years); From 141° solar longitude (for a description of this unit see *Sidiropoulos and Muller* [2015]) in Martian year (MY) 24 through 82° solar longitude in MY 27. In addition, the temperature and wind fields are specified on 25 vertical atmospheric levels. These levels are defined by a specific percentage of surface pressure, or “sigma” levels. For much of our analysis, we focus on the 9 sigma level (83% of surface pressure, $\approx$6 mbar). On the one hand, this is at an altitude sufficiently high to avoid most issues of topography and dust storms (the strong effects of dust storms on observational temperature data are well documented in *Conrath et al.* [2000]). On the other hand, the 9 sigma level was also sufficiently low so as to be well within the region where the reanalysis’ observational data are most accurate [*Montabone et al.*, 2014]. We also give some more limited results at other pressure levels and these yield quite similar results; see Table 4.

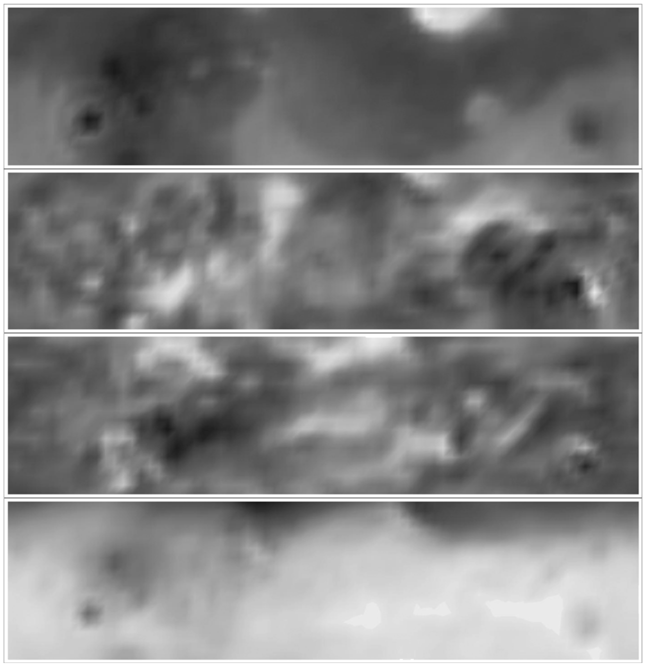

Figure 1. Gray-shade renderings of the MACDA reanalysis for the 6 Martian hour, 141° solar longitude in Martian year (MY) 24, on the atmospheric level with 83% of surface pressure. (top to bottom) The renderings are for top to bottom respectively surface pressure (p), meridional wind (v), zonal wind (u), and temperature (T).

For the purposes of analysis, the original spherical grid was simplified by taking a cylindrical projection of the region between the ±45° latitudes (Gray-shade renderings of these grids are shown in Figure 1). Not only does this projection allow us to focus our analysis on the region where the observational data are most concentrated, but it is also close enough to the equator so as to be relatively insensitive to latitudinal variations in pixel size [see *Lovejoy and Schertzer*, 2011, Appendix]. The theoretically more elegant method based on spherical harmonics was not used since as we show below, the reanalyses are strongly anisotropic in the horizontal so that analyses must be performed separately in zonal and meridional directions. Analysis of the higher latitudes is left for future studies, but the basic statistical laws (e.g., scaling exponents) are likely to be the same [see, e.g., *Lovejoy and Schertzer*, 2010].

The exception to our treatment of the free atmospheric fields was the surface pressure field. Since its variability is strongly dependent on the topography, rather than analyzing the surface pressure directly, we analyzed the pressure anomalies with respect to the pressure averaged over the entire reanalysis period. The same was done for the terrestrial European Centre for Medium Range Weather Forecasts (ECMWF) reanalysis since the closest existing previous analysis [*Lovejoy and Schertzer*, 2011] was of the geopotential height and hence was not directly comparable.

Finally, we mention that the MACDA reanalysis data are no longer the only Martian reanalysis. Recently, the Ensemble Mars Atmosphere Reanalysis System (EMARS) appeared [*Greybush et al.*, 2014]. EMARS is partially based on more recent observational data from the Mars Climate Sounder observational temperature limb profiles [see *Kleinböhl et al.*, 2009]. In addition, this reanalysis is built on a different model, the GFDL Mars GCM [see *Wilson and Hamilton*, 1996], and a more advanced assimilation algorithm, the Local Ensemble Transform Kalman Filter (LETKF) [see *Hunt et al.*, 2007]. However, at the time of writing, this reanalysis was not publicly available.

3. Fourier-Space Spectral Scaling

3.1. Theoretical Considerations

Lovejoy and Schertzer [2011] presented a systematic analysis of the Earth's atmosphere at 700 mb (≈3 km, using the European Centre for Medium Range Weather Forecasts (ECMWF) Reanalysis (interim) and 365 consecutive daily reanalyses of key atmospheric variables: temperature, wind (all components), geopotential height, and humidity. In order to systematically compare these to the MACDA reanalyses, we start with spectral analysis which is both familiar and sensitive to breaks in the scaling. The spectrum is a second-order statistic, whereas a full statistical analysis requires all the moments; this is postponed until section 4 which provides a direct analysis of the turbulent fluxes that are responsible for the intermittency.

We begin our theoretical discussion of spectral scaling with a field $F(\bar{r})$ of a position vector $\bar{r}$ (extending to the time dimension is straightforward). The Fourier transform of this field is expressed as follows:

$$\tilde{F}\left(\bar{k}\right) = \int e^{i\bar{k}\cdot\bar{r}} F\left(\bar{r}\right) \mathrm{d}\bar{r}, \tag{1}$$

where $\bar{k}$ is the wave vector dual to $\bar{r}$; we take F as real so that it satisfies $\tilde{F}\left(\bar{k}\right)=\tilde{F}^*\left(-\bar{k}\right)$ ("*" indicates complex conjugate, the tilda indicates Fourier transform). With this transform, we can then write an expression for the power spectral density P:

$$\left\langle \tilde{F}\left(\bar{k}\right)\tilde{F}^*\left(\bar{k}'\right)\right\rangle = \delta\left(\bar{k}+\bar{k}'\right)P\left(\bar{k}\right). \tag{2}$$

As with convention, the brackets refer to "statistical averaging", "δ" is the Dirac function. For finite and real data F, the spectral density P is thus proportional to the ensemble average of the modulus squared of the Fourier transform of F. Empirically, fast Fourier techniques (with Hanning windows) are used to estimate the Fourier transforms in equation (2). This is followed by an ensemble averaging, which we estimate by averaging over the entire data set.

For systems that are statistically isotropic, P is solely dependent on the modulus of $\bar{k}$: $P\left(\bar{k}\right)=P\left(|\bar{k}|\right)$. Now, consider an isotropic "zoom" (i.e., a standard "blowup") by a scale $\lambda > 1$ in real space: $\bar{r}\rightarrow\lambda\bar{r}$, which is the inverse of the Fourier-space "blowdown": $\bar{k}\rightarrow\lambda^{-1}\bar{k}$. If the system is "self-similar" (a system that is both isotropic and scaling), then the relation between small and large scales is independent of a characteristic size. This implies the following power law relation between small scales $\bar{k}$ and larger scales $\lambda^{-1}\bar{k}$:

$$P\left(\lambda^{-1}\bar{k}\right)\approx\lambda^{s}P\left(\bar{k}\right). \tag{3}$$

The solution to the above can be expressed in a power law form:

$$P\left(|\bar{k}|\right)\approx|\bar{k}|^{-s}. \tag{4}$$

Note that we have purposely taken a methodical approach to this theoretical discussion so far, as we will shortly relax the isotropic assumption by replacing $\bar{k}$ with a scale function that respects scaling symmetries, to allow for nonself-similar and anisotropic scaling systems.

It is common in spectral analysis to evaluate an "isotropic spectrum" $E(k)$ (with $k=|\bar{k}|$). This spectrum is calculated by an integration over all space: in one dimension, $E(k)=2P(k)$, in two dimension, $E(k)=2\pi kP(k)$, and in three dimensions, $E(k)=4\pi k^2P(k)$. In empirical analysis, where one is constrained by finite sample size, one can integrate over all angles to improve the estimate of $E(k)$ (via noise reduction), by using

$$E(k)=\int_{\delta S_k}P(\bar{k}')\mathrm{d}\bar{k}', \tag{5}$$

where S_k is defined as the d-dimensional sphere and δS_k, the integration region, is its boundary (we have ignored the factor N, the number of degrees of freedom from the Dirac function in equation (2)). In one dimension, the end points of the interval is from k to $k+\delta k$ (reduces to $E(k)=2\langle|F(k)|^2\rangle$). In two dimensions, the integral is done over a circle radius k (reduces to $E(k)=2\pi\langle|F(k)|^2\rangle$). In three dimensions, the integration is done over a spherical shell radius k (reduces to $E(k)=4\pi\langle|F(k)|^2\rangle$). Using equation (5) and the expression for the power spectral density in equation (4), we can express the spectrum in a power law form:

$$E(|\bar{k}|)\approx|\bar{k}|^{-\beta};\ \beta=s-d+1. \tag{6}$$

Based on equation (6), the spectrum obeys a theoretical power law dependence. Therefore, we empirically test for scaling of the field F, by examining the power law form of the field's spectrum. (Note, we ignore the d-dependent factors.)

3.2. Spatial Spectra

In Figure 2, we show $P(\bar{k})$ for the surface pressure (p), meridional wind (v), zonal wind (u), and temperature (T) variables of the Earth and Martian reanalyses (for the surface pressure we analyzed the anomalies, not the pressure directly). The Martian reanalysis data were taken over a period of 3 Martian years and at 83% of surface pressure (≈6 mb, close to the corresponding terrestrial levels discussed below). The Earth data used for this analysis were taken from the European Centre for Medium Weather Forecast (ECMWF) reanalysis products [*Lovejoy and Schertzer*, 2011], for the year 2006 and at 69% of surface pressure (700 mb). To make the scaling more evident in Figures 3–6, the spectra were also averaged over 10 logarithmic spaced bins.

From Figure 2, it can be seen that although the lines of constant $P(\bar{k})$ are roughly circular at high wave numbers corresponding to isotropy at scales of about one or two reanalysis pixels—that at the smaller wave numbers (near the centre, i.e., corresponding to the larger real-space scales), the contours are elliptical, with the ellipse

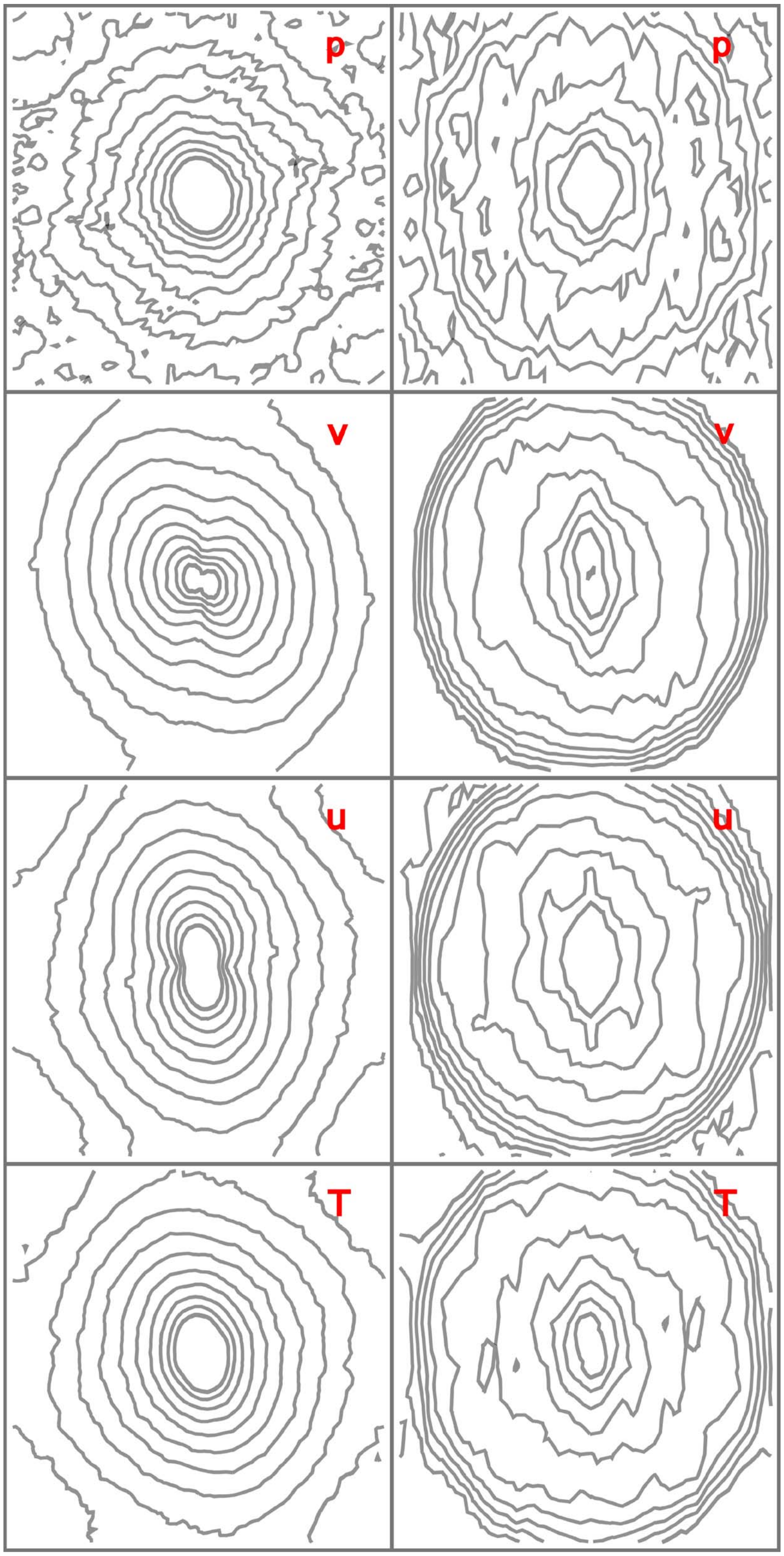

Figure 2. Contour Plots of log *P* for (left column) Earth and (right column) Mars. Figures 2 (left column) and 2 (right column) within the plots are k_x and vertical direction is k_y. From Figures 2 (first row) to 2 (fourth row), the plots are for surface pressure (*p*), meridional wind (*v*), zonal wind (*u*), and temperature (*T*). Due to the 2:1 aspect ratio (which compensates for the 2:1 change in range of k_x, with respect to k_y), a circle the diameter of the square in the plots corresponds to isotropy at the 2 pixel scale.

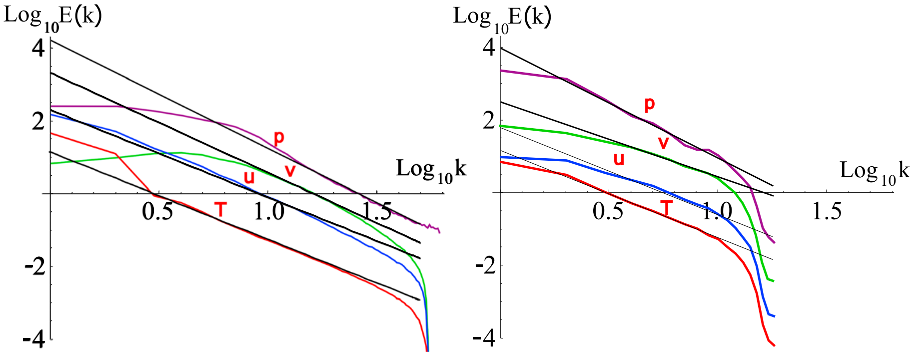

Figure 3. The zonal spectra of (left) Earth and (right) Mars as functions of the nondimensional wave numbers for the p (purple), v (green), u (blue), and T (red) fields. The data for Earth were taken at 69% atmospheric pressure for 2006 between latitudes ±45°. The data for Mars were taken at 83% atmospheric pressure for Martian Year 24 to 26 between latitudes ±45°. Figure 3 (left) shows the zonal spectra of Earth, and the reference lines have absolute slopes, from top to bottom (β): 3.00, 2.40, 2.40, and 2.75 (for p, v, u, and T, respectively). Figure 3 (right) shows the zonal spectra of Mars, and the reference lines have absolute slopes, from top to bottom (β): 3.00, 2.05, 2.35, and 2.35 (for p, v, u, and T, respectively). The spectra have been rescaled to add a vertical offset for clarity and $k = 1$ corresponds to the half circumference of the respective planets. The vertical offsets in $\mathrm{Log}_{10}E(k)$ are (p, v, u, and T, respectively): −1, 0, −0.3, and −0.5 for Earth and 2.7, 1.35, 0.6, and 0 for Mars.

axes aligned along the coordinate directions (NS and EW). This suggests that the scaling exponents in the zonal and meridional directions are quite different (the largest structures are typically wider in the zonal than meridional direction). It is therefore important to estimate the one-dimensional spectra $E(k_x)$, $E(k_y)$, which are obtained by integrating out the conjugate wave numbers:

$$\begin{aligned} E(k_x) &= \int P(k_x, k_y)\mathrm{d}k_y \\ E(k_y) &= \int P(k_x, k_y)\mathrm{d}k_x. \end{aligned} \tag{7}$$

Figures 3 and 4 compare $E(k_x)$ and $E(k_y)$; we see that the fields exhibit scaling below 3000 km and 2500 km, for Earth and Mars, respectively (equivalent to nondimensional distances 3000/20,000 = 0.15 and 2500/10,700 = 0.23, respectively). Performing regressions, we obtain estimates of the β values; see Table 2. With the exception of the meridional wind (v) in the zonal direction, we see that all the exponents are nearly the same on the two planets. Also note that in accord with Figure 2 and with the findings by *Lovejoy and Schertzer* [2011], (with the exception of the surface pressure anomaly) that all the fields have strong (scaling)

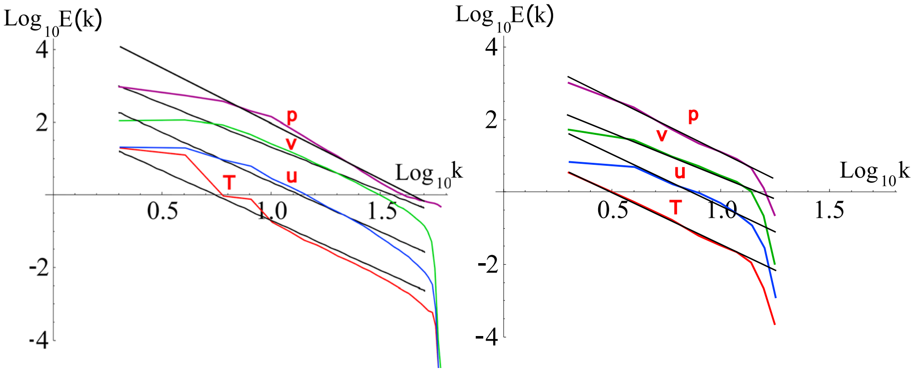

Figure 4. The same as Figure 3 except for the meridional spectra of (left) Earth and (right) Mars for the p (purple), v (green), u (blue), and T (red) fields. The same data as Figure 3 were used for the spectra of both planets. Figure 4 (left) shows the meridional spectra of Earth, and the reference lines have absolute slopes, from top to bottom (β): 3.00, 2.75, 2.75, and 2.40 (for p, v, u, and T, respectively). Figure 4 (right) shows the meridional spectra of Mars, and the reference lines have absolute slopes, from top to bottom (β): 3.00, 2.40, 2.80, and 2.80 (for p, v, u, and T, respectively). The spectra have been rescaled to add a vertical offset for clarity and $k = 1$ corresponds to the half circumference of the respective planets. The vertical offsets in $\mathrm{Log}_{10}E(k)$ are (p, v, u, and T, respectively): −1, 0, −0.4, and −0.5 for Earth and 2.2, 1.4, 0.4, and 0 for Mars.

Table 2. β and H Values for Mars and Earth[a]

	p		v		u		T	
	Earth	Mars	Earth	Mars	Earth	Mars	Earth	Mars
β_{EW}	3.00	3.00	2.75	2.05	2.40	2.35	2.40	2.35
β_{NS}	3,00	3.00	2.40	2.40	2.75	2.80	2.75	2.80
β_{τ}	2.00	2.00	2.00	2.00	2.00	2.00	1.80	1.80
H_{EW}	1.12	1.11	0.96	0.60	0.77	0.75	0.77	0.76
H_{NS}	1.13	1.18	0.78	0.80	0.95	0.99	0.95	1.00

[a] The β values are taken from the fits on Figures 3, 4, and 7. The H values are calculated with the respective $K(q)$ estimates and the β values, in accordance with equation (23). The $K(q)$ estimates are taken from the C_1, α estimates in Table 3. For the spatial analysis (EW and NS), the β and hence H estimates of Earth are good fits up to 3000 km and the corresponding estimates for Mars are good fits up to 2500 km.

NS-EW anisotropies. For most of the exponents (see, however, Table 3, the C_1, α estimates) there is no conventional error analysis because the exact exponent values depend on the precise ranges used for the fitting (recall that at the lowest wave numbers the scaling is broken due to the deterministic effects that are the focus of the usual approaches, whereas at the highest wave numbers the scaling is broken due to the hyperviscosity). However, we have put reference lines and these are plausible to within ±0.05 for the spectral exponents. The reader may judge the log-log linearity (scaling) of the data with respect to the lines; we believe that the procedure is as accurate as is warranted by the data.

To understand this anisotropy, we turn to generalized scale invariance (GSI) [*Schertzer and Lovejoy*, 1985]; in this case, P satisfies the following scale symmetry:

$$P(\lambda^{-G}\bar{k}) = \lambda^{s}P(\bar{k}), \tag{8}$$

where s is the scaling exponent of the density, λ is a scaling ratio, G is the anisotropy generator, and λ^{-G} is the operator that (anisotropically) reduces the scale of the vector k by a factor λ. When anisotropy varies only with scale but not position, G is a matrix ("linear" GSI). If the axes of the anisotropy are parallel to the coordinate axes (as in Figure 2), then G is a diagonal matrix:

$$G = \begin{pmatrix} 1 & 0 \\ 0 & H_y \end{pmatrix}; \lambda^{-G} = \begin{pmatrix} \lambda^{-1} & 0 \\ 0 & \lambda^{-H_y} \end{pmatrix}, \tag{9}$$

Table 3. Flux Planet Comparison[a]

		p		v		u		T	
		Earth	Mars	Earth	Mars	Earth	Mars	Earth	Mars
C_1	EW	0.119 ± 0.002	0.100 ± 0.001	0.077 ± 0.005	0.074 ± 0.002	0.084 ± 0.006	0.076 ± 0.003	0.09 ± 0.01	0.086 ± 0.005
	NS	0.122 ± 0.001	0.168 ± 0.002	0.077 ± 0.005	0.078 ± 0.001	0.084 ± 0.006	0.076 ± 0.001	0.09 ± 0.01	0.088 ± 0.003
α	EW	2.01 ± 0.02	2.17 ± 0.02	1.90 ± 0.006	1.95 ± 0.01	1.85 ± 0.01	1.95 ± 0.04	1.85 ± 0.01	1.962 ± 0.007
	NS	2.15 ± 0.02	2.20 ± 0.02	1.90 ± 0.006	1.94 ± 0.01	1.85 ± 0.01	1.946 ± 0.002	1.85 ± 0.01	1.88 ± 0.02
L_{eff} Ratio	EW	1.97	3.48	0.5	0.88	0.32	0.77	0.4	0.67
	NS	1.64	0.84	0.5	0.56	0.32	0.66	0.4	0.36
Error (%)	EW	0.7	0.77	0.35	0.4	0.31	0.53	0.28	0.71
	NS	2.14	2.68	0.35	0.69	0.31	0.76	0.28	0.9

[a] For Mars, C_1, α, and the L_{eff} ratio estimates are estimated with fits of Mars flux estimates under 6000 km for the zonal direction (EW) and 3000 km for the analysis in the meridional direction (NS), at 83% of surface pressure and over a period of 3 Martian years (MY 24–MY 26). For Earth, C_1, α, and the L_{eff} ratio estimates are estimated with fits of Earth flux estimates under 5000 km for both the zonal direction (EW) and meridional direction (NS), at 69% of surface pressure and over a period of 1 Earth year (2006). The spreads in the parameters for Mars are over three samples of the data, each spanning a Martian year. In contrast, the spreads in the parameters for Earth are over the data for east-west and north-south directions and time. C_1 and α values are estimated directly from fitting equation (26) to the various flux estimates at different pressure levels. L_{eff} is estimated by obtaining the λ intercept of the flux plots and determining its ratio with respect to the half circumference of Mars. The error is calculated with the log regression method outlined in equation (28).

where H_y is a ratio of scaling exponents in the meridional to zonal directions and $H_y = 1$ (the identity) corresponds to isotropy (equation (3)). Note that this simple expression (equation (9)) for the exponential of a matrix only holds when G is diagonal. The solution of the functional equation (8) is

$$P(\bar{k}) \propto ||\bar{k}||^{-s}, \tag{10}$$

where $||\bar{k}||$ is the (nondimensional) "scale function," which is adopted to replace the vector modulus (in equation (4)) for anisotropic and scaling systems. This "scale function" $||\bar{k}||$ satisfies the following functional scaling relation:

$$||\lambda^{-G}\bar{k}|| = \lambda^{-1}||\bar{k}||. \tag{11}$$

At this point, we would like to note that we are considering only the scale by scale anisotropy of a scalar quantity; this stands, in contrast, to traditional approaches to anisotropy in the meteorological literature [e.g., *Hoskins et al.*, 1983] which analyzes a vector quantity anisotropy (e.g., the wind) at a particular (fixed) scale (e.g., the resolution of the model).

The easiest, "canonical" solution to equation (11) (with G given by equation (9)) is

$$||\bar{k}|| = \left((k_x/k_s)^2 + (k_y/k_s)^{2/H_y}\right)^{1/2}, \tag{12}$$

where k_s is the "sphero- wave number," a wave number that corresponds to approximately isotropic (uniform) contours (Note that equation (12) is expressed as a dimensionless scale function; one may obtain a dimensional one by multiplying the right-hand side by k_s). It is worth emphasizing that this scale function solution is only the simplest in the class of solutions to equations (10) and (11), for more general solutions that involve essentially an arbitrary "unit ball," for a review, see chapters 6 and 7 of *Lovejoy and Schertzer* [2013].

Formally speaking, testing equations (9)–(11) is a difficult statistical parameter estimation problem, see, e.g., *Lewis et al.* [1999] for the "Scale Invariant Generator" technique which is useful in cases where G is an arbitrary 2×2 matrix. But we adopt a simpler approach since G is diagonal in our case we use the one-dimensional spectra in both directions (zonal and meridional), the two-dimensional angle-integrated (isotropic) spectrum all obtained from the two-dimensional spectral density P.

Accordingly, we first test equations (9)–(12) from the one-dimensional zonal (east-west) and meridional (north-south) spectra, $E_{\mathrm{EW}}(k_x)$ and $E_{\mathrm{NS}}(k_y)$, which can be expressed as follows:

$$\begin{aligned} E_{\mathrm{EW}}(k_x) &= \int P(k_x, k_y)\mathrm{d}k_y = A_x\left(\frac{k_x}{k_s}\right)^{-\beta_{\mathrm{EW}}}; \beta_{\mathrm{EW}} = s - H_y; s > H_y \\ E_{\mathrm{NS}(k_y)} &= \int P(k_x, k_y)\mathrm{d}k_x = A_y\left(\frac{k_y}{k_s}\right)^{-\beta_{NS}}; \beta_{\mathrm{NS}} = \frac{s-1}{H_y}; s > 1, \end{aligned} \tag{13}$$

where A_x, A_y are dimensionless constants with order of magnitude unity (note that these constants depend on the exact solution to equation (10) and recal that the canonical scale function (equation (12)) is only one of a class of solutions). A key implication of equation (13) is that (if $s > H_y$, $s > 1$) one may obtain the following simple relation between exponents:

$$H_y = \frac{\beta_{\mathrm{EW}} - 1}{\beta_{\mathrm{NS}} - 1}. \tag{14}$$

Note that the overall variance contribution from all structures smaller than a given wave number k is provided by the integration of $E(k)$ from k to infinity. We can therefore utilize this fact to obtain a one to one space-space relationship (in implicit form) between the directional wave numbers, k_x and k_y:

$$\int_{k_x}^{\infty} E_x(k'_x)\mathrm{d}k'_x = \int_{k_y}^{\infty} E_y(k'_y)\mathrm{d}k'_y \tag{15}$$

If $\beta_x > 1$, $\beta_y > 1$, then equation (15) (with (13) and (14)) reduces to:

$$k_y = k'_s\left(\frac{k_x}{k'_s}\right)^{H_y}, \tag{16}$$

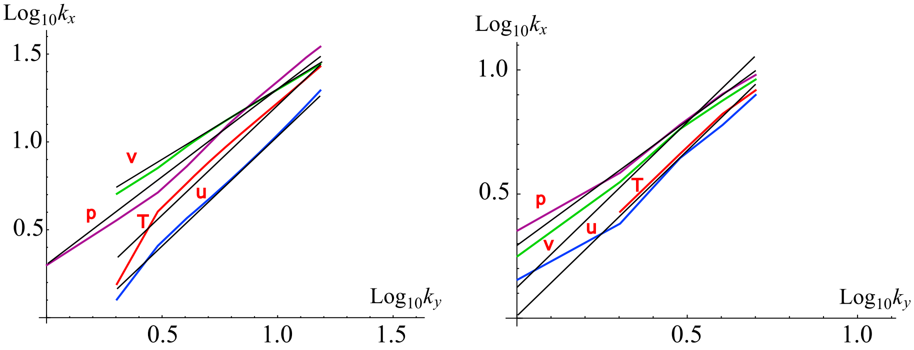

Figure 5. The empirical space-space relations for p (purple), v (green), u (blue), and T (red) of (left) Earth and (right) Mars, calculated using the implicit relation equation (equation (15)).The same data as Figure 3 were used for the space-space relations of both planets. Figure 5 (left) shows the space-space relations for Earth and the reference lines have slopes from top to bottom, 1/0.8, 1, 0.8, and 0.8. Figure 5 (right) shows the space-space relations for Mars and the reference lines have slopes from top to bottom, 1, 0.75, and 0.75.

where $k'_s \approx k_s$ (since $A_x \approx A_y \approx H_y \approx 1$). We can now easily test for scaling anisotropy by directly using the k_x, k_y space-space relation (i.e., the relation between k_x and k_y implicitly defined by the general equation (15), in the case of scaling, explicitly given in equation (16) obtained from the one-dimensional spectra and then check if the power law form is roughly observed (equation (16)). Therefore, we have plotted from the one-dimensional spectra, the space-space relation of the zonal (east-west) and meridional (north-south) winds in Figure 5. In this figure, we have drawn scaling fit lines with slopes 1.25 (which is the best fit regression line based on the zonal wind (u) data) and slope $1/1.25 = 0.80$ which closely matches the meridional wind (v) data (in both cases, the slopes $= 1/H_y$) and theoretical predictions; isotropic scaling would lead to lines with slopes 1; only the pressure anomaly appears to be isotropic. It is worth noting that the scaling of the space-space relations in Figure 5 is better than the individual zonal (east-west) and meridional (north-south) spectra (Figures 3 and 4); one reason for this is that the individual spectra suffer from some residual deviations to scaling caused by the hyperviscosity at small scales (i.e., the unphysical reanalysis dissipation mechanism).

3.2.1. Angle-Integrated (Isotropic) Spectra

Whatever the explanation for the anisotropy, the angle-integrated spectral exponents are still of interest (equation (5)). If the spectral density P is anisotropic, then

$$\begin{aligned} E(k) &\approx k^{-\beta_l};\ \beta_l = \min(\beta_{\text{EW}}, \beta_{\text{NS}});\ k \ll k_s \\ E(k) &\approx k^{-\beta_h};\ \beta_h = \max(\beta_{\text{EW}}, \beta_{\text{NS}});\ k \gg k_s \end{aligned} \tag{17}$$

with β_h the high and β_l the low wave number spectral exponents. One implication of equation (17) is that it predicts a scaling break in the spectrum at k_s. Since this break is a consequence of the isotropic integration, the break is simply a spurious methodological artifact and does not imply a true break in the spectral density: referring to equations (10) and (12), the full two-dimensional spectral density P is perfectly scaling.

The exponents β_{EW} and β_{NS} are related by equation (14), and so for $H_y < 1$, we can explicitly express the low wave number exponent as either β_{EW} or β_{NS} under the following conditions:

$$\beta_l = \min(\beta_{\text{EW}}, \beta_{\text{NS}}) = \begin{matrix} \beta_{\text{EW}};\ \beta_{\text{EW}} > 1 \\ \beta_{\text{NS}};\ \beta_{\text{NS}} < 1 \end{matrix} \tag{18}$$

with a corresponding equation for the high wave number spectral exponent β_h, which uses the maximum rather than the minimum function (and the converse inequalities resulting from the condition $H_y > 1$).

As mentioned before, the spectra in this analysis are based on anisotropic fields. However, if we are mindful of the potential issues, we may still approximate isotropy and integrate over all angles to obtain $E(k)$. This method has the advantage of providing cleaner estimates as the angle-based integral reduces noise. Furthermore, since k_s is very close to the wave number of the one pixel scale (see Figure 2) we only examine wave numbers under the condition $k < k_s$. Thus, we do not expect a break in the scaling for our data since the condition $k < k_s$ ensures that we only observe the low wave number β_l exponent (equations (17) and (18)).

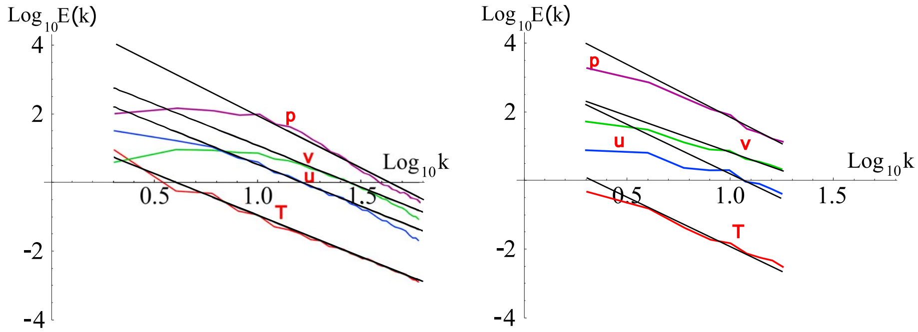

Figure 6. The angle-integrated "isotropic" spectra of Earth and Mars estimated integrating the power spectral density over annuli. The same data as Figure 3 was used for the spectra of both planets. (left) The isotropic spectra of Earth and the reference lines have absolute slopes, from top to bottom (β): 3.00, 2.40, 2.40, and 2.40 (for p (purple), v (green), u (blue), and T (red), respectively). (right) The isotropic spectra of Mars and the reference lines have absolute slopes, from the top to bottom (β): 3.00, 2.05, 2.35, and 2.35 (for p, v, u, and T, respectively). The spectra have been rescaled to add a vertical offset for clarity and $k = 1$ corresponds to the half circumference of the respective planets. The vertical offsets in Log$_{10}E(k)$ are (p, v, u, and T, respectively): −5.5, −0.5, −0.9, and −1.2 for Earth and −0.4, −1.6, −2.3, and −4 for Mars. All the reference lines are from the 1-D spectra (Figures 3 and 4) and the anisotropic theory, equation 17.

Empirically, the approximations in equation (17) are better at smaller wave numbers. Therefore, we obtain good estimates of the spectra by simply calculating P with numerical Fourier transforms over the available 120×60 pixel grids and subsequently performing integrals over circular annuli, keeping only the wave numbers below 30 (the smaller end of the wave number range). Due to the 2:1 aspect ratio, the above mentioned procedure is the same as integrating over ellipses with an aspect ratio of 2:1; this compressed integration region yields qualitatively similar results (equation (17)) but generates a faster convergence to the power law form $k^{-\beta_I}$.

We show the angle-integrated spectra for the four atmospheric variables for Mars and the Earth in Figure 6. As with the other spectra, they were nondimensionalized by the half circumference (i.e., $k = 1$ corresponds to half a circumference; for example, wave numbers 10 times higher correspond to structures 10 times smaller). For the Earth, the scaling is generally excellent and the reference lines—with slopes chosen to satisfy equation (18) (i.e., *not* the results of regression) are also accurate. For the Earth notable exceptions are the sharp breaks for meridional (north-south) wind and surface pressure, near $k^{-1} \approx 0.1$ (≈2000 km); k is the wave number nondimensionalized by the circumference. For Mars the scaling is also typically quite good, with the notable exception of the zonal (east-west) wind, which possesses a break at around $k^{-1} \approx 0.2$ (≈2000 km).

There are no theories that predict different scaling in the NS and EW directions, and it is highly significant, that Figure 2 shows that the spectra at the one pixel scale (the largest wave numbers) are close to being isotropic. Isotropy at the one pixel scale is an artifact of the hyperviscosity required by the reanalysis numerics. At the same time, all the fields that have a stronger global scale NS gradient than EW gradients (u, v, and T but not the pressure anomaly) display scaling exponents whose magnitude essentially allows them to adjust from a large NS global scale gradient to a single pixel isotropy. As argued in *Lovejoy and Schertzer* [2011], this anisotropy is a reanalysis artifact, a feature neither of terrestrial nor Martian dynamics. This interpretation is bolstered by the near isotropy of the turbulent fluxes that govern the wind and temperature fields (section 3.4 below). The exception—confirming the rule—is the pressure anomaly field that is isotropic throughout, a consequence of the fact that the large scale NS-EW *anomalies* have very similar magnitudes.

3.3. Discussion

The theoretical prediction that atmospheric statistics should respect a scale invariance principle is indeed quite general. Indeed, the more general (nonlinear) forms of generalized scale invariance (GSI), in which the notion of scale not only is anisotropic and a function of size but also varies from one location to another, would be difficult to falsify. However, in this paper, we validate a far more restrictive form of GSI in which the directions of anisotropy are fixed: they are independent of both size and location and are even parallel to the usual coordinate axes (this is the self-affine special case of linear GSI in which the generator is a diagonal matrix). The log-log plots displaying linearity over wide ranges of scale validate this restrictive form of GSI. Had the lines failed to be linear (power laws) over significant ranges, this special form would have been falsified. In actual fact, the analyses already falsify GSI over the smallest and largest scales. This is comforting since for obvious reasons, the spectra are not expected to be power laws at small hyperviscous scales, whereas at the largest scales, the theory only requires that the scaling is confined to scales much smaller than the outer planetary scales. The small wave number deviations from log-log linearity also falsify GSI at the very largest scales, but again, this shows the sensitivity of the analysis method to breaks in the symmetry. In summary, the analysis already shows that GSI is false exactly where it is expected to be false.

It is sometimes thought that symmetry principles such as scaling are so general that they are not useful. This type of skepticism animated debate in the 1840s about another symmetry principle: conservation of energy (it was not understood as a symmetry principle until Noether's theorem in the twentieth century). At the time, the principle of conservation of energy was considered to be too speculative and top physics journals rejected papers by Helmholtz, Kelvin and others dealing with the subject.

3.4. Temporal Spectra

On Earth, all atmospheric fields undergo a drastic transition in their statistical properties at scales of 5–10 days. At first the transition was ascribed to synoptic scale "migratory pressure systems" [*Panofsky and van der Hoven*, 1955], then to the "synoptic maximum" [*Kolesnikov and Monin*, 1965], later to baroclinic instabilities [*Vallis*, 2010]. At the same time, there was a parallel theorization of τ_w as the lifetime of planetary structures that separated two scaling regimes *Lovejoy and Schertzer* [1986].

This behavior is clearest and the significance of the transition most obvious if we consider the (real space) fluctuations $\Delta F(\Delta t)$ for a fluctuation over a field F with time interval Δt:

$$\Delta F(\Delta t) = \phi \Delta t^{H}, \tag{19}$$

where ϕ is the turbulent flux (or power of the flux) and H the fluctuation exponent (sometimes called the "nonconservation exponent": for quasi Gaussian processes it is equal to the Hurst exponent). Since (essentially by its definition as a statistically scale invariant flux) the mean of the turbulent flux is independent of scale ($\langle\phi\rangle \approx$ constant), we have $\langle\Delta F(\Delta t)\rangle \approx \Delta t^{H}$ so that when $H > 0$, fluctuations grow with scale whereas when $H < 0$, they decrease. When $H > 0$, the series $F(t)$ is like a "drunkard's walk" (indeed, the latter has $H = 1/2$), with $F(t)$ and $F(t-\Delta t)$ tending to be more and more different as Δt increases (i.e., the differences $\Delta F(\Delta t) = F(t) - F(t-\Delta t)$ tend to grow with Δt). On the contrary, when $H < 0$, successive fluctuations tend to cancel out with large positive excursions being nearly canceled out by following negative ones (and visa versa). When $H < 0$, rather than differences, $\Delta F(\Delta t)$ must be defined using anomalies (i.e., the signal with its long term mean removed). When these anomalies are averaged over longer and longer periods Δt, they tend to converge to zero (and the signal itself to its long term mean) at a rate determined by H. This type of short time growing (diverging with Δt since $H > 0$, $\Delta t < \tau_w$) and then long time decreasing (converging with Δt since $H < 0$, $\Delta t > \tau_w$), behavior is a mathematical expression of the idea that while "The weather is what you get, the climate is what you expect." However, as pointed out in *Lovejoy et al.* [2013], after durations of 100 years or so (the preindustrial period) there is another transition to an $H > 0$ regime (due to anthropogenic warming, the transition is only about 20 years in the industrial epoch: *Lovejoy et al.* [2013]). Therefore, there are three fundamental regimes—not two. The low frequency regime continues to the frequencies associated with the ice ages (50–100 kyrs) and is most naturally associated with the climate. The middle regime was baptized "macroweather" since it is statistically well reproduced by deterministic weather models and stochastic turbulent (cascade) models (the "Fractionally Integrated Flux" model, see *Lovejoy and Schertzer* [2013], chapter 10, and *Lovejoy and de Lima* [2015]).

So what is the origin of the transition at $\tau_w \approx 5-10$ days? The conventional explanation *Vallis* [2010] is that it is associated with baroclinic instabilities, but precise models (based on the Eady mechanism) make many unrealistic homogeneity assumptions, and in any case, it diverges in the tropics (where the Coriolis force vanishes) whereas the empirical τ_w has only small latitudinal variations. However, given the wide range scaling displayed in the previous sections (i.e., scaling that holds with fixed exponents over a wide range of scales), it is natural to seek turbulent explanations, in this case based on the Kolmogorov law for fluctuations in the wind (Δv): $\Delta v(\Delta x) = \epsilon^{1/3}\Delta x^{1/3}$, where ϵ is the energy flux from large to small scales (sometimes called the "energy rate density" since the units are m^2/s^3 = W/Kg). The key point is that while the original Kolmogorov law was isotropic, due to the stratification, it could not possibly hold to large scales.

In contrast, the anisotropic generalizations (GSI) only predict it to hold in the horizontal with a different exponent (from the buoyancy variance flux) governing the vertical statistics, thereby allowing the Kolmogorov law

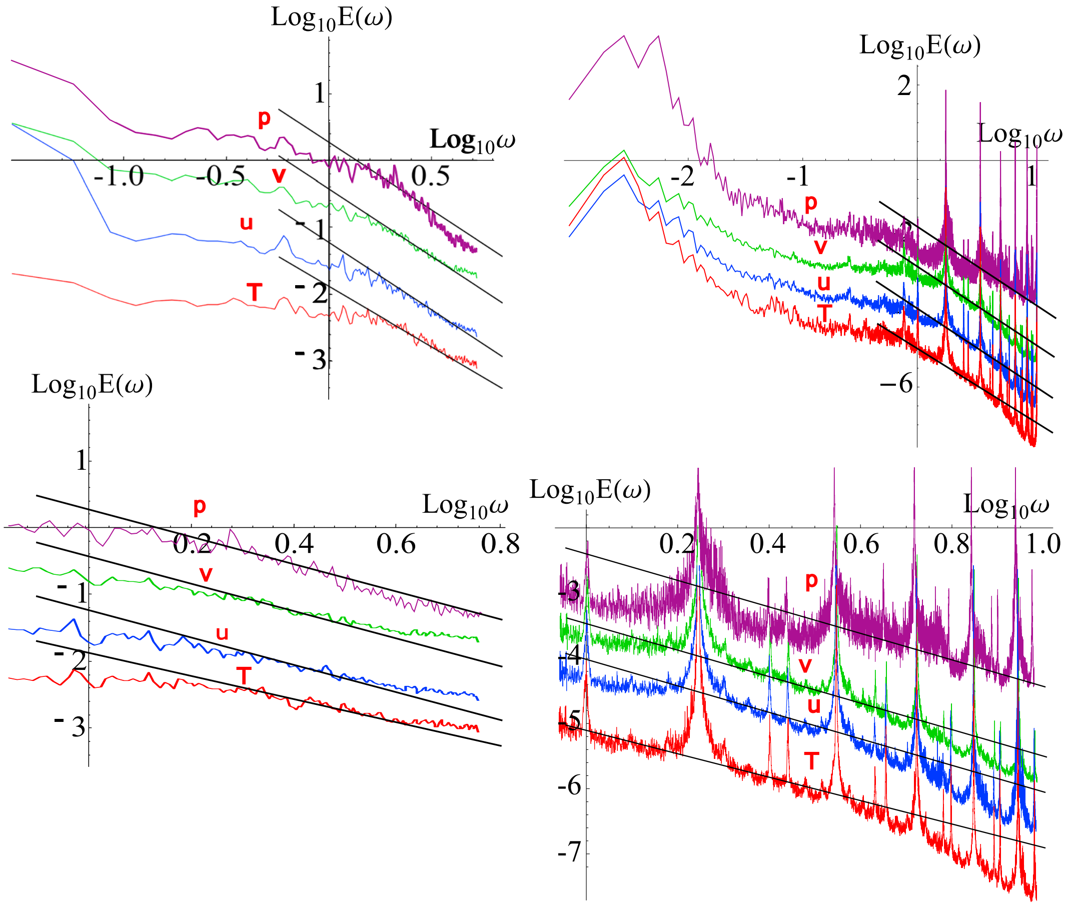

Figure 7. The frequency spectrum with ensemble averaging of (left column) Earth and (right column) Mars for p (purple), v (green), u (blue), and T (red) atmospheric fields, nondimensionalized to $\omega = 1$ at the respective "weather-macroweather" transitional frequency (τ_w) of both planets (10 days for Earth and 1.8 sols for Mars). The same data as Figure 3 were used for the spectra of both planets. (top left) The frequency spectrum of Earth in the year 2006, at a resolution of 1 day. From Figure 7 (right column), the reference lines have absolute slopes (β): 2.0, 2.0, 2.0, and 1.8 (for $\omega > (1.8 \text{ sols})^{-1}$, "weather" region, of p, v, u, and T, respectively). (bottom left) A blowup of the high-frequency (weather) regime for the frequency spectrum of Earth. (top right) The frequency spectrum of Mars in Martian year (MY) 24–26, at a resolution of 0.2 hours. (bottom right) A blowup of the high-frequency (weather) regime for the frequency spectrum of Mars. The vertical offsets in $\text{Log}_{10}E(\omega)$ are (p, v, u, and T, respectively): −2.3, 0.6, 0.6, and −0.8 for Earth and 1.2, 0.2, −1.5, and −0.6 for Mars.

to hold in the horizontal up to planetary scales. In this case, *Lovejoy and Schertzer* [2010] showed that ϵ can easily be estimated from the incoming solar forcing (≈1 mW/Kg) and directly yields the characteristic transition period—the lifetime of planetary sized structures: $\tau_w = \epsilon^{-1/3} L_w^{2/3}$, where L_w is the planetary scale (the largest great circle distance, on the Earth, this is 20,000 km). Since the ocean is also a turbulent fluid—but with surface currents having ϵ about 10^5 times smaller than the atmosphere—the same theory predicts a break there at $(10^5)^{1/3} \approx 30$ times longer, i.e., about 1 year, a prediction confirmed by ocean temperature spectra [*Lovejoy and Schertzer*, 2012]. The final evidence in favor of the turbulent explanation is the prediction of an equivalent weather-macroweather transition on Mars at ≈1.8 sols in *Lovejoy et al.* [2014]. This prediction was based on estimating $\epsilon \approx 40$ mW/Kg from the Martian incoming solar flux combined with the thickness of the Martian atmosphere; it was well verified using Viking Lander as well as the same MACDA reanalysis data as analyzed here. Purely empirically, the shorter time scale on Mars can be estimated using the typical Martian horizontal wind (70 m/s) compared with 27 m/s on Earth, combined with the smaller Martian radius. Just as on Earth the lifetime and hence transition time scale has some latitudinal and altitude dependence, so it also does on Mars: the transition scale of 1.8 sols compared to about 8.5 days on Earth—is an average.

The existence of wide scale range horizontal scaling is not the same as a classical “inertial range.” Recall that an inertial range is a range with no energy flux sources or sinks, it does not exist in the real atmosphere. However—at least on Earth—the energy inputs (solar radiation modulated by clouds and albedo) and energy sinks (infrared radiances modulated by clouds and other turbulent fields) are both scaling so that the dynamics are nevertheless scale invariant [*Lovejoy et al.*, 2009].

In *Lovejoy et al.* [2014], only the temperature and wind fields were analyzed and this over a single Martian year. Therefore, we now complete the analysis by extending it to both wind components and to the surface temperature field and out to the full length of the MACDA reanalysis: 3 Martian years (allowing notably an estimate of the amplitude of the annual cycle). We conduct the analysis using the same steps outlined in section 3.2, with the frequency ω replacing the wave number k. Figure 7 shows the spectra of the four atmospheric variables of Mars and Earth, respectively, in the time domain. The data for Earth span an Earth year (2006) with a temporal resolution of a day. The data for Mars span 3 Martian years (MY 24–26) with a temporal resolution of 2 h. The geographical regions used for both Martian and terrestrial analyses are the same as the range used for the spatial analyses.

Figure 7 shows the comparison where the frequencies have been nondimensionalized by the weather/macroweather transition scale with τ_w taken as 10 days and 1.8 sols. The reference lines for wind and temperature have the same low- and high-frequency reference slopes as in *Lovejoy et al.* [2014], and the surface pressure anomaly has the value $\beta = 2$ (see Table 2).

Due to the limited low frequency range of data, we were unable to precisely locate the transition point between the (lower frequency) “climate” regime and the (intermediate frequency) “macroweather” regime for both planets. As seen in Figure 7 (top left), the transition between climate and macroweather for Earth is not visible at all since (industrial period) it is at frequency of the order of (20 years)$^{-1}$. However, for Mars, the results as illustrated in Figure 7 top right indicate that there is a possible transition point at about (40 days^{-1}). But this “transition” point could also indicate the presence of a low frequency harmonic on the order of a year and/or a rather (spectrally) wide annual cycle. Therefore, we could not definitively identify this point as a climate “transition point.”

4. Real-Space Atmospheric Statistics: Fluxes and Fluctuations

4.1. Discussion

The spectral exponent is a second-order statistic; it is simply one of an infinite hierarchy that are needed for a full statistical description, especially for the intermittency. These other moments are most conveniently estimated in real space and can be fruitfully analyzed in the framework of multiplicative cascades. Starting with equation (19) but for the spatial separation Δr replacing the temporal lag Δt, taking q^{th} powers and ensemble averaging, we obtain the q^{th} order “structure function”:

$$\langle \Delta F(\Delta r)^q \rangle = \langle \phi_{\Delta r}^q \rangle \Delta r^{qH}. \tag{20}$$

In general, we have

$$\langle \phi_{\Delta r}^q \rangle \propto \Delta r^{-K(q)}, \tag{21}$$

where $K(q)$ is a convex function of the moment q; hence, we have

$$\langle \Delta F(\Delta r)^q \rangle \propto \Delta r^{\xi(q)}; \xi(q) = qH - K(q), \tag{22}$$

where $\xi(q)$ is the structure scaling exponent of moment q.

A useful relation is obtained by considering the second-order ($q = 2$) moment which is related to the spectral exponent β via:

$$\beta = 1 + \xi(2) = 1 + 2H - K(2). \tag{23}$$

This relation is derived from the Wiener-Khintchin theorem: the spectrum is the Fourier transform of the autocorrelation function. This relation will be useful in estimating H from β (estimated earlier) and $K(q)$ determined below. Using the values obtained for β in section 3 and the flux in section 4, we calculated the values for H, which are shown in Table 2.

4.2. Predictions of the Multiplicative Cascade Theory

The multiplicative cascade theory describes the theoretical characteristics of the intermittent flux, in the form of a multiscaling law:

$$\langle \phi_{\lambda'}^{q} \rangle = \lambda'^{K(q)}; \lambda' = \frac{L_{\mathrm{eff}}}{\Delta r}, \tag{24}$$

where $\langle \phi_{\lambda}^{q} \rangle$ is the statistical average of a flux of moment order q and a scale ratio λ'. When Greek λ' equals to 1; $\Delta r = L_{\mathrm{eff}}$, the "effective" outer scale of the cascade and so all the fluxes of different moments converge at this scale. Physically, this scale of convergence corresponds to where the cascade begins and so is described as the "effective outer scale" of the cascade.

In empirical analyses, the outer scale is an important empirical parameter that must be determined from the data. Since we expect the outer scale to be close to the size of the planet—largest great circle distance—we can define the scale ratio λ with respect to a convenient reference scale: $L_{\mathrm{ref}} = L_w = \pi R$, where R is the planetary radius. In this case, the empirical flux moments obey

$$\langle \phi_{\lambda}^{q} \rangle = \left(\frac{\lambda}{\lambda_{\mathrm{eff}}} \right)^{K(q)}; \ \lambda_{\mathrm{eff}} = \frac{L_{\mathrm{ref}}}{L_{\mathrm{eff}}}, \ \lambda = \frac{L_{\mathrm{ref}}}{\Delta r}. \tag{25}$$

Finally, without further theoretical considerations, the exponent function $K(q)$ represents an infinite number of parameters (one for each moment q). This is unmanageable—either empirically or theoretically. However, there exist stable, attractive universality classes so that a priori we may expect the function $K(q)$ to follow the two parameter universal form *Schertzer and Lovejoy* [1987]:

$$K(q) = \frac{C_1}{\alpha - 1}(q^{\alpha} - q), \tag{26}$$

with the "Levy index" α characterizing the degree of multifractality and in the range 0 to 2 (the former corresponding to the monofractal "beta modal," the latter to the lognormal multifractal model). The parameter C_1 (≥ 0) describes the intermittency near the mean flux, which is the sparseness of the field that gives the dominant contribution to the calculation of the mean flux, $C_1 = K'(1)$. The dimension of the corresponding set is defined as the difference between the dimension of the space in which the set is embedded and the fractal codimension. At lower fractal codimensions (near zero), the structure becomes more uniform and less intermittent. Similarly, at higher fractal codimensions, the structure becomes more sparse; it is more intermittent. Thus, the codimension parameter quantifies the intermittency.

4.2.1. Spatial Flux Analysis

To analyze the spatial flux of a multiplicative cascade, we can divide both sides of equation (19) by its ensemble average to obtain

$$\phi'_{\Lambda} = \frac{\phi_{\Lambda}}{\langle \phi_{\Lambda} \rangle} = \frac{\Delta f}{\langle \Delta f \rangle}, \tag{27}$$

where Λ is the scale ratio of λ_{eff} to the smallest spatial scale l (here, the grid size) and ϕ'_{Λ} is the nondimensional flux normalized so that $\phi'_{\Lambda} = 1$.

The fluctuation Δf can be estimated in various ways, for example, by absolute first or second differences (1-D series) or (2-D) by finite difference Laplacians (the latter was used here). Once the field of normalized fluxes at the finest resolution ϕ'_{Λ} has been estimated from the fluctuations, it can then be degraded (by straightforward averaging) to yield the fluxes at intermediate resolutions with scale ratio $\lambda \leq \Lambda$.

Performing regressions on the log-log plots of the average flux estimates ($M_q = \langle \phi_{\lambda}'^{q} \rangle$) of varying moments and scale would allow one to obtain the flux characteristic parameters, that were outlined in section 4.2 (note, due to equations (24) and (25), all regressions must be constrained to go through a single λ intercept at $\lambda = \lambda_{\mathrm{eff}}$). The first parameter—the outer scale of the cascade—can be obtained by using the fact that $\lambda_{\mathrm{eff}} = \frac{L_{\mathrm{ref}}}{L_{\mathrm{eff}}}$ at $\lambda = \lambda_{\mathrm{eff}}$, i.e. at the $\lambda' = 1$ intercept. The $K(q)$ function may be obtained by taking the regressions slopes of the log-log plots, which are estimates of $K(q)$ at different q that are fitted to equation (24). Finally, from $K(q)$, we can estimate C_1 and α either from a nonlinear regression to the universal form (equation (26)) or more simply from the easy to verify relations: $C_1 = K'(1)$ and $\alpha = K''(1)/K'(1)$.

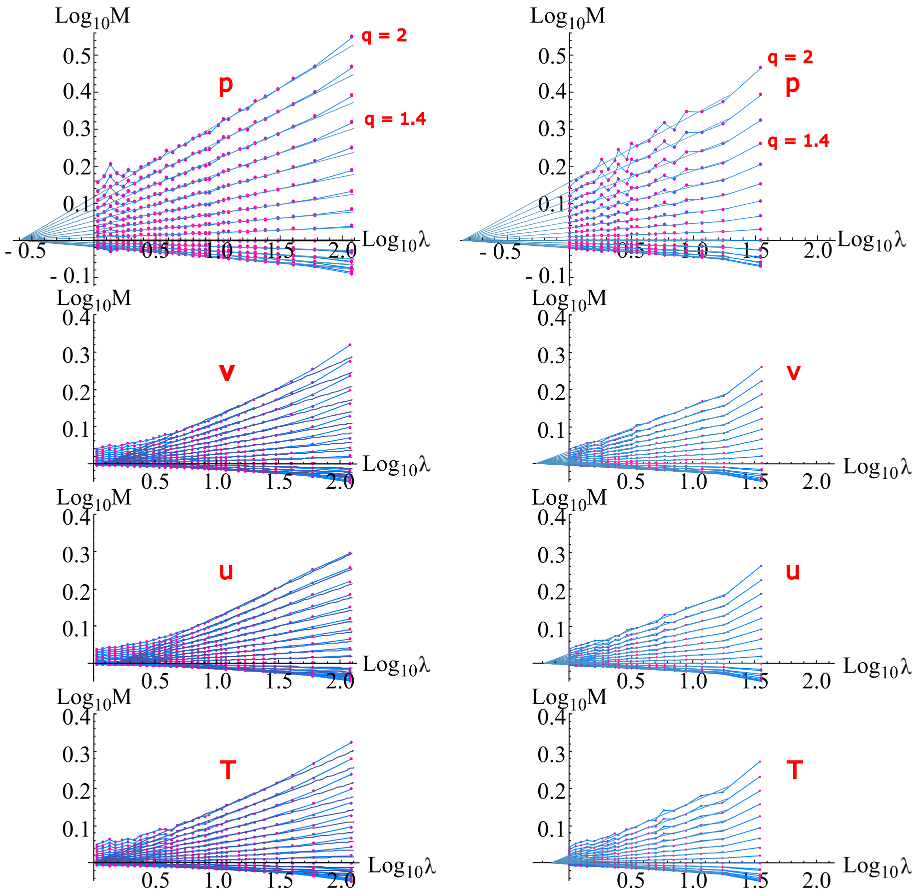

Figure 8. The analysis for the flux for both (left column) Earth and (right column) Mars in the zonal (EW) direction. The same data as Figure 3 was used for the flux of both planets. The fluxes were estimated using finite difference Laplacians. Figure 8 (left column) shows the zonal flux for Earth and the curves are the moments $q = 0, 0.1, 0.2$ ...1.9, 2.0. Figure 8 (right column) shows the zonal flux for Mars and the curves are the moments $q = 0, 0.2, 0.4$ ...2.0. For both figures, the dots are the actual empirical values, and the straight lines are the log-log regression of equation (26) (i.e., with slopes $K(q)$) forced to go through a common point (the external scale ratio λ_{eff}). For Earth, the slopes were estimated with empirical values below 5000 km. For Mars, the slopes were estimated with empirical values below 6000 km. Finally, the reference scale, $\lambda = 1$, corresponds to the half circumference of the respective planets. The terrestrial u, v, and T analyses are from *Lovejoy and Schertzer* [2011].

Figures 8 and 9 show the results of the analysis conducted in the zonal (EW) and meridional (NS) direction respectively on the same data as for the spectral analysis, and Figure 9 for the corresponding meridional analysis. Again, as with the spectra analysis, four atmospheric variables are as follows: surface pressure (p), zonal wind (u), meridional wind (v), and temperature (T) were compared between Earth and Mars. The dots in Figures 8 and 9 represent the empirical estimates for the fluxes that were evaluated using equation (27). As indicated on the plots, the flux estimates (M_q) are evaluated from the highest scale (half circumference of the planet) to the lowest scale (highest resolution of data) and for moments $q = 0, 0.2, 0.4 \ldots, 2.0$.

The lines indicate the fits based on the multiplicative cascade model (see equation (26)) and the accuracy of the fits was quantified by the percentage residual of the fitted log-log regression lines. The residuals (Δ) were estimated as

$$\Delta = \left| \log_{10}(M_q) - K(q)\log_{10}\left(\frac{\lambda}{\lambda_{\text{eff}}}\right) \right|. \tag{28}$$

The residuals were averaged over all sampled moments q and over the fitted scale range. This average was subsequently converted to a percent deviation (δ), where $\delta = 100(10^{\Delta} - 1)$. Using this error estimation, the regressions were found to be good fits up to a scale corresponding to nondimensional distances of about $\lambda^{-1} = k^{-1} = 0.25$ (≈5000 km) for fluxes on Earth and about $\lambda^{-1} = k^{-1} = 0.6$ (≈6000 km) for fluxes on Mars (see Table 3).

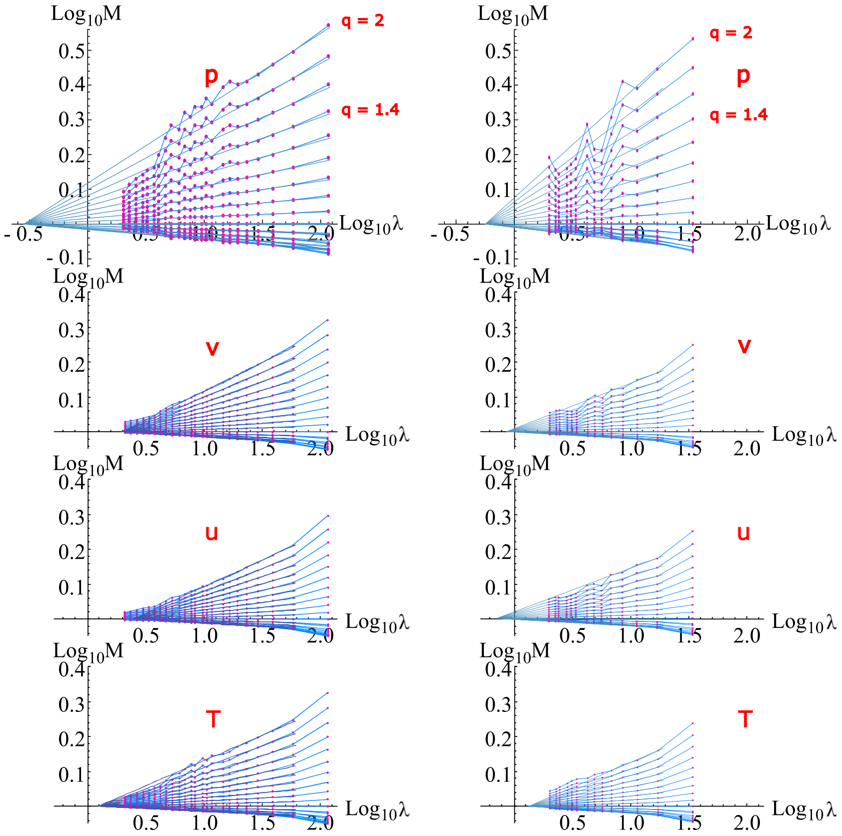

Figure 9. Same as Figure 8 but for the meridional (NS) analysis. The data in the NS direction span 90° in latitude, but the reference scale, $\lambda = 1$, was kept at the half circumference of the respective planets. (left column) The meridional flux for Earth and the slopes were estimated with empirical values below 5000 km. (right column) The meridional flux for Mars, and the slopes were estimated with empirical values below 3000 km. The terrestrial u, v, and T analyses are from *Lovejoy and Schertzer* [2011].

Comparing the results between the two planets (Table 3), one finds that the flux exponents C_1, α, and nondimensional outer scale ratio λ_{eff} in the zonal and meridional directions are very similar for both planets.

The key conclusions are that the intermittency (cascade) exponents are virtually identical on the two planets and also in the NS-EW directions so that unlike the fields u, v, and T that were strongly anisotropic (flattened in the EW direction at large scales), the fluxes were nearly isotropic at all scales. This supports the interpretation discussed earlier that the fields themselves displayed spurious anisotropy due to the imposed strong meridional gradients (the gradients do not directly affect the fluxes which are estimated from the Laplacians).

Focusing solely on Mars, we also conducted a flux analysis in the zonal and meridional directions across various surface pressure levels and tabulated the flux characteristics parameters in Table 4, for the zonal and meridional directions, respectively. With only the zonal wind (u), meridional wind (v), and temperature (T), we found that there are only small variations in the intermittency exponents in the vertical, and these could be artifacts of the model. A possible reason is that the different vertical pressure levels use observational data with different resolutions, and at progressively higher altitudes, the reanalysis data become more and more model based. Another possible explanation is the inadequacy of the hydrostatic approximation in the reanalyses. The reason for suspecting the hydrostatic approximation is that the vertical exponents of the horizontal wind and other fields are not realistic. Indeed, in *Lovejoy et al.* [2010], it is shown that the *vertical* spectrum of the horizontal wind in dropsonde data is nearly identical to the *isobaric* reanalysis spectrum that is incorrectly interpreted as a horizontal spectrum. Finally, one should note that at the surface, the data are affected by the topography, which again could lead to a variation in the flux parameters over lower vertical levels.

Table 4. Flux Mars Level Comparison[a]

		v			u			T		
Percent of Surface Pressure		100%	83%	46%	100%	83%	46%	100%	83%	46%
C_1	EW	0.107 ± 0.001	0.074 ± 0.002	0.072 ± 0.002	0.087 ± 0.002	0.076 ± 0.003	0.074 ± 0.001	0.079 ± 0.003	0.086 ± 0.005	0.095 ± 0.004
	NS	0.086 ± 0.003	0.078 ± 0.001	0.077 ± 0.001	0.122 ± 0.002	0.076 ± 0.001	0.072 ± 0.001	0.095 ± 0.005	0.088 ± 0.003	0.088 ± 0.001
α	EW	2.05 ± 0.01	1.95 ± 0.01	1.875 ± 0.006	1.908 ± 0.004	1.95 ± 0.04	1.90 ± 0.02	1.83 ± 0.01	1.962 ± 0.007	2.09 ± 0.01
	NS	1.838 ± 0.009	1.94 ± 0.01	1.882 ± 0.009	1.96 ± 0.02	1.946 ± 0.002	1.86 ± 0.02	1.83 ± 0.01	1.88 ± 0.02	1.994 ± 0.003
$Ł_{eff}$ ratio	EW	0.43	0.88	0.98	0.69	0.77	0.92	1.38	0.67	1
	NS	0.46	0.56	0.43	0.32	0.66	0.35	0.47	0.36	0.45
Error (%)	EW	1	0.4	0.42	0.55	0.53	0.51	0.78	0.71	0.55
	NS	1.16	0.69	0.62	1.67	0.76	0.67	1.3	0.9	1.16

[a] The C_1, α, and the L_{eff} ratio Mars parameter estimates are estimated with fits of the flux estimates of different atmospheric pressure on Mars under 6000 km for the zonal direction (EW) and under 3000 km for the meridional direction (NS). The spreads in the parameters estimates for Mars are over three samples of the data, each spanning a Martian year. C_1 and α values are estimated directly from fitting equation (26) to the various flux estimates at different pressure levels. L_{eff} is estimated by obtaining the λ intercept of the flux plots and determining its ratio with respect to the half circumference of Mars. The error is calculated with the log regression method outlined in equation (28).

5. Conclusions

The study of other planets usually benefits from relevant knowledge of the Earth; in this paper we inverted the process effectively using knowledge of the Martian atmosphere to give us greater confidence in terrestrial turbulent laws, allowing us to see Earth as a member of a larger ensemble. In the case of the Martian atmosphere, up until now this has largely been at the level of comparing deterministic mechanisms that aim at explaining Martian dynamics over relatively small ranges of scales from the size of the planet down to scales a factor of four or five smaller in horizontal. These mechanistic comparisons have focused either on similarities—for example, on the Martian version of the Hadley circulation or on the high-level Martian jets—or on the differences, notably the role of dust in directly heating the middle and upper Martian atmosphere, or the strong role of topography and tides on Mars or of water in its various phases on Earth.

However, on both planets, the Reynolds numbers are greater than 10^{11} so that the flows are unstable and turbulent with dissipation only occurring at centimetric (Mars) or millimetric (Earth) scales. If we nondimensionalize the distances l by the largest great circle distance (the half circumference, L_w), then in rough terms the deterministic mechanisms may adequately explain the dynamics from scales $l/L_w = \lambda^{-1} = 1$ to ≈ 0.2 or 0.1, but we are left to deal with the range 0.1 to 10^{-8} (Mars) and 0.1 to 10^{-9} (Earth). The only framework that can deal succinctly with such large ranges is scale invariance, especially when generalized to account for scaling anisotropy (vertical stratification or EW/NS scaling anisotropy) and scaling intermittency (multifractality). Although there is a now a considerable body of evidence in favor of this on Earth (see the extensive review by *Lovejoy and Schertzer* [2013]), the claim is sufficiently strong that it requires strong evidence, hence, the significance of studying Mars. Already, *Lovejoy et al.* [2014] showed how to nondimensionalize the fundamental weather/macroweather transition scales using the lifetimes of planetary structures (themselves inferred by solar forcing), finding that Martian and terrestrial temperature and wind spectra could then be superposed over wide ranges of scale (with the partial exception of the diurnal and annual cycles that were somewhat different on the two planets).

In this paper we extend this temporal statistical comparison in several ways examining the temperature, zonal and meridional wind and surface pressure anomaly fields in space as well as time. First, we completed the temporal spectral analyses by including surface pressure anomalies and extending the previous analyses over 1 Martian year to 3 Martian years obtaining both better statistics but also a clearer idea of the surprisingly broad Martian annual cycle. However, the main originality here is the systematic comparison of the spatial spectra (using the same methodology as described in *Lovejoy and Schertzer* [2011] for analysis of the terrestrial ECMWF reanalyses) as well as the turbulent fluxes. In the spatial domain, the exponents are again very close with notably the intermittency parameters being nearly identical with only the pressure anomaly field having slightly different intermittency parameters (the intermittency near the mean, C_1, see Table 3).

The spectral and related (real space) fluctuation exponents β and H again were extremely close (nearly within experimental error of each other)—in both the zonal and meridional directions (which were different) the only exception being the meridional velocity and this only in the zonal direction (e.g., $\beta_{v,\mathrm{EW}} = 2.75$ (Earth), 2.05 (Mars) and $H_{v,\mathrm{EW}} = 0.96$ (Earth), 0.60 (Mars).

But even this single exception—the zonal exponent of the meridional wind—may reflect more the limitations of the reanalyses than on real differences between the planets. This is because—as on the Earth—the reanalyses (with the exception of the pressure anomaly field) reflect the strong meridional gradients and are therefore strongly anisotropic at the largest (planetary) scale—with aspect ratios of about 2:1 in the zonal direction yet at the grid scales they are nearly perfectly isotropic. In *Lovejoy and Schertzer* [2011] it was argued that this scaling anisotropy (i.e., the different EW and NS exponents) was simply an artifact of the imposition of nearly perfect isotropy at the (essentially arbitrary) grid scale, that this horizontal stratification was a reflection of the way the model systematically transformed strong north-south gradients into roughly isotropic hyperdissipation scale gradients. The interpretation that this anisotropy was spurious was bolstered by the fact that no theory of turbulence predicts anisotropy in the horizontal scaling and that the turbulent fluxes (that directly reflect the dynamics and are insensitive to boundary conditions) were found to be essentially isotropic.

The finding that Mars and Earth are often dissimilar when considered from the vantage point of deterministic mechanisms describing the very largest scales but are nearly identical as concerns the statistics of the remaining wide ranges of scales gives additional strong support for the view espoused and reviewed in

Lovejoy and Schertzer [2013] that—in accord with the expectations of classical turbulence theory—there are indeed high-level turbulent laws that emerge from the chaos of huge numbers of interacting structures at very high Reynolds numbers. This follows since the dynamical equations are essentially the same (the core being the Navier-Stoke equations), and the result is expected to be insensitive to the boundary conditions (In fact, it turns out that—at least as concerns their topographic boundary conditions—that the two planets are also quite similar: both have scaling topography—*Gagnon et al.* [2006] (Earth), *Landais et al.* [2015] (Mars) with similar exponents at least at scales above 10 km). The success of the high-level laws in explaining terrestrial and Martian statistics therefore provides a strong case for using the high-level laws for understanding, modeling, and forecasting the fields [see, e.g., *Lovejoy et al.*, 2015].

Acknowledgments

This work was initiated as part of Chen's final year undergraduate project in the McGill University physics department, Lovejoy's participation was unfunded so that there were no conflicts of interest. Muller's participation was partially supported by grant STFC MSSL Consolidated grant ST/K000977/1. The data used in this study can be accessed from the MACDA repository at http://browse.ceda.ac.uk/browse/badc/mgs/data/macda/v1-0 (for Mars atmospheric data) and the ECMWF repository at http://apps.ecmwf.int/datasets/data/interim-full-daily/?levtype=ml (for Earth atmospheric data).

References

Christensen, P. R., et al. (2001), Mars Global Surveyor Thermal Emission Spectrometer experiment: Investigation description and surface science results, *J. Geophys. Res.*, *106*(E10), 23,823–23,871, doi:10.1029/2000JE001370.

Conrath, B. J., J. C. Pearl, M. D. Smith, W. C. Maguire, P. R. Christensen, S. Dason, and M. S. Kaelberer (2000), Mars Global Surveyor Thermal Emission Spectrometer (TES) observations: Atmospheric temperatures during aerobraking and science phasing, *J. Geophys. Res.*, *105*(E4), 9509–9519, doi:10.1029/1999JE001095.

Forget, F., F. Hourdin, R. Fournier, C. Hourdin, O. Talagrand, M. Collins, S. R. Lewis, P. L. Read, and J.-P. Huot (1999), Improved general circulation models of the Martian atmosphere from the surface to above 80 km, *J. Geophys. Res.*, *104*(E10), 24,155–24,175, doi:10.1029/1999JE001025.

Gagnon, J. S., S. Lovejoy, and D. Schertzer (2006), Multifractal Earth topography, *Non. Processes Geophys.*, *13*, 541–570.

Greybush, S. J., R. J. Wilson, E. Kalnay, Y. Zhao, R. Hoffman, and T. Nehrkorn (2014), *Ensemble Mars Reanalysis System (EMARS), Presented at the Fifth International Workshop on the Mars Atmosphere: Modelling and Observations*, Jointly sponsored by the Centre National d'Etudes Spatiales and the European Space Agency, Oxford, U. K.

Hollingsworth, J. L., and J. R. Barnes (1996), Forced stationary planetary waves in Mars's winter atmosphere, *J. Atmos. Sci.*, *53*, 438–448, doi:10.1175/1520-0469(1996)053.

Holloway, J. L., and S. Manabe (1971), Simulation of climate by a global general circulation model, *Mon. Weather Rev.*, *99*, 335–370, doi:10.1175/1520-0493(1971)099.

Hoskins, B. J., I. N. James, and G. H. White (1983), The shape, propagation and mean-flow interaction of large-scale weather systems, *J. Atmos. Sci.*, *40*, 1595–1612, doi:10.1175/1520-0469(1983)040<1595:TSPAMF>2.0.CO;2.

Hourdin, F. (1992), A new representation of the absorption by the CO2 15-μm band for a Martian general circulation model, *J. Geophys. Res.*, *97*(E11), 18,319–18,335, doi:10.1029/92JE01985.

Hourdin, F., P. L. Van, F. Forget, and O. Talagrand (1993), Meteorological variability and the annual surface pressure cycle on Mars, *J. Atmos. Sci.*, *50*, 3625–3640, doi:10.1175/1520-0469(1993)050.

Hunt, B. R., E. J. Kostelich, and I. Szunyogh (2007), Efficient data assimilation for spatiotemporal chaos: A local ensemble transform Kalman filter, *Physica D*, *230*(1–2), 112–126, doi:10.1016/j.physd.2006.11.008.

Kleinböhl, A., et al. (2009), Mars Climate Sounder limb profile retrieval of atmospheric temperature, pressure, and dust and water ice opacity, *J. Geophys. Res.*, *114*, E10006, doi:10.1029/2009JE003358.

Kolesnikov, V. N., and A. S. Monin (1965), Spectra of meteorological field fluctuations, *Izv. Russ. Acad. Sci. Atmos. Oceanic Phys., Engl. Transl.*, *1*, 653–669.

Landais, F., F. Schmidt, and S. Lovejoy (2015), Universal multifractal Martian topography, *Nonlin. Processes Geophys. Discuss.*, *2*, 1007–1031, doi:10.5194/npgd-2-1007-2015.

Leovy, C. (2001), Weather and climate on Mars, *Nature*, *412*, 245–249, doi:10.1038/35084192.

Leovy, C., and Y. Mintz (1969), Numerical simulation of the atmospheric circulation and climate of Mars, *J. Atmos. Sci.*, *26*, 1167–1190, doi:10.1175/1520-0469(1969)026.

Lewis, G. M., S. Lovejoy, D. Schertzer, and S. Pecknold (1999), The scale invariant generator technique for parameter estimates in generalized scale invariance, *Comp. Geosci.*, *25*, 963–978, doi:10.1016/S0098-3004(99)00061-8.

Lewis, S. R., P. L. Read, B. J. Conrath, J. C. Pearl, and M. D. Smith (2007), Assimilation of thermal emission spectrometer atmospheric data during the Mars Global Surveyor aerobraking period, *Icarus*, *192*(2), 327–347, doi:10.1016/j.icarus.2007.08.009.

Lewis, S. R., D. P. Mulholland, P. L. Read, L. Montabone, R. J. Wilson, and M. D. Smith (2016), The solsticial pause on Mars: 1. A planetary wave reanalysis, *Icarus*, *264*, 456–464, doi:10.1016/j.icarus.2015.08.039.

Lorenc, A. C., R. S. Bell, and B. Macpherson (1991), The Meteorological Office analysis correction data assimilation scheme, *Q. J. R. Meteorol. Soc.*, *117*, 59–89, doi:10.1002/qj.49711749704.

Lovejoy, S., and M. I. P. de Lima (2015), The joint space-time statistics of macroweather precipitation, space-time statistical factorization and macroweather models, *Chaos*, *25*, 75410, doi:10.1063/1.4927223.

Lovejoy, S., and D. Schertzer (1986), Scale invariance in climatological temperatures and the spectral plateau, *Ann. Geophys. B*, *4*, 401–410.

Lovejoy, S., and D. Schertzer (2010), Towards a new synthesis for atmospheric dynamics: Space-time cascades, *Atmos. Res.*, *96*, 1–52, doi:10.1016/j.atmosres.2010.01.004.

Lovejoy, S., and D. Schertzer (2011), Space-time cascades and the scaling of ECMWF reanalyses: Fluxes and fields, *J. Geophys. Res.*, *116*, D14117, doi:10.1029/2011JD015654.

Lovejoy, S., and D. Schertzer (2012), Stochastic and scaling climate sensitivities: Solar, volcanic and orbital forcings, *Geophys. Res. Lett.*, *39*, L11702, doi:10.1029/2012GL051871.

Lovejoy, S., and D. Schertzer (2013), *The Weather and Climate: Emergent Laws and Multifractal Cascades*, Cambridge Univ. Press, Cambridge, U. K.

Lovejoy, S., D. Schertzer, V. Allaire, T. Bourgeois, S. King, J. Pinel, and J. Stolle (2009), Atmospheric complexity or scale by scale simplicity?, *Geophys. Res. Lett.*, *36*, L01801, doi:10.1029/2008GL035863.

Lovejoy, S., A. F. Tuck, and D. Schertzer (2010), The Horizontal cascade structure of atmospheric fields determined from aircraft data, *J. Geophys. Res.*, *115*, D13105, doi:10.1029/2009JD013353.

Lovejoy, S., D. Schertzer, and D. Varon (2013), Do GCM's predict the climate...or macroweather?, *Earth Syst. Dyn.*, *4*, 1–16, doi:10.5194/esd-4-1-2013.

Lovejoy, S., J. P. Muller, and J. P. Boisvert (2014), On Mars too expect macroweather, *Geophys. Res. Lett.*, *41*, 7694–7700, doi:10.1002/2014GL061861.

Lovejoy, S., L. del Rio Amador, and R. Hebert (2015), The Scaling LInear Model (SLIM): Using scaling to forecast global scale macroweather from months to decades, *Earth Syst. Dynam. Discuss.*, *6*, 489–545, doi:10.5194/esdd-6-489-2015.

Mintz, Y. (1965), Very long-term global integration of the primitive equations of atmospheric motion: (An experiment in climate simulation), *WMO Tech Notes*, *66*(30), 20–36.

Montabone, L., K. Marsh, S. R. Lewis, P. L. Read, and M. D. Smith (2014), The Mars Analysis Correction Data Assimilation (MACDA) Dataset V1.0, *Geosci. Data J.*, *1*, 129–139, doi:10.1002/gdj3.13.

Morcrette, J. J., L. Smith, and Y. Fouquart (1986), Pressure and temperature dependence of the absorption in longwave radiation parametrizations, *Contrib. Atmos. Phys.*, *5*(9), 455–469.

Panofsky, H. A., and I. van der Hoven (1955), Spectra and cross-spectra of velocity components in the mesometeorological range, *Q. J. R. Meteorol. Soc.*, *81*, 603–606, doi:10.1002/qj.49708135010.

Pollack, J. B., C. B. Leovy, Y. H. Mintz, and W. Van Camp (1976), Winds on Mars during the Viking season: Predictions based on a general circulation model with topography, *Geophys. Res. Lett.*, *3*(8), 479–482, doi:10.1029/GL003i008p00479.

Schertzer, D., and S. Lovejoy (1985), Generalised scale invariance in turbulent phenomena, *Phys. Chem. Hydrodyn. J.*, *6*, 623–635.

Schertzer, D., and S. Lovejoy (1987), Physical modelling and analysis of rain and clouds by anisotropic scaling of multiplicative processes, *J. Geophys. Res.*, *92*, 9693–9714, doi:10.1029/JD092iD08p09693.

Smith, M. D., J. L. Bandfield, and P. R. Christensen (2000), Separation of atmospheric and surface spectral features in Mars Global Surveyor Thermal Emission Spectrometer (TES) spectra, *J. Geophys. Res.*, *105*(E4), 9589–9607, doi:10.1029/1999JE001105.

Sidiropoulos, P., and J. P. Muller (2015), On the status of orbital high-resolution repeat imaging of Mars for the observation of dynamic surface processes, *Planet. Space Sci.*, *117*, 207–222, doi:10.1016/j.pss.2015.06.017.

Vallis, G. (2010), Mechanisms of climate variability from years to decades, in *Stochastic Physics and Climate Modeling*, edited by P. W. T. Palmer, pp. 1–34, Cambridge Univ. Press, Cambridge, U. K.

Wilson, R. J., and K. Hamilton (1996), Comprehensive model simulation of thermal tides in the Martian atmosphere, *J. Atmos. Sci.*, *53*, 1290–1326, doi:10.1175/1520-0469(1996)053.